Progressive Retinal Image Registration via Global and Local Deformable Transformations

1st Yepeng Liu
School of Computer Science
Wuhan University
Wuhan, China
yepeng.liu@whu.edu.cn

2nd Baosheng Yu
School of Computer Science
The University of Sydney
Sydney, Australia
baosheng.yu@sydney.edu.au

3rd Tian Chen
School of Computer Science
Wuhan University
Wuhan, China
tian.chen@whu.edu.cn

4th Yuliang Gu
School of Computer Science
Wuhan University
Wuhan, China
yuliang_gu@whu.edu.cn

5th Bo Du
School of Computer Science
Wuhan University
Wuhan, China
dubo@whu.edu.cn

6th Yongchao Xu*
School of Computer Science
Wuhan University
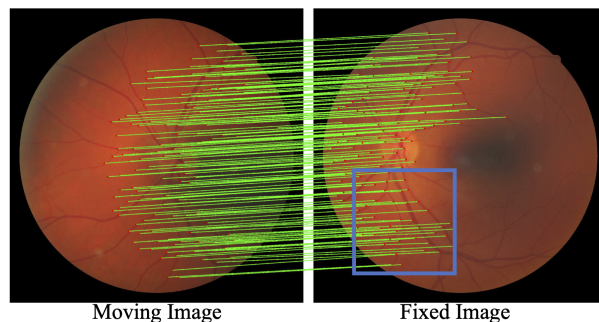Wuhan, China
yongchao.xu@whu.edu.cn

7th Jun Cheng
Institute for Infocomm Research
*A*STAR*
Singapore
cheng_jun@i2r.a-star.edu.sg

Abstract—Retinal image registration plays an important role in the ophthalmological diagnosis process. Since there exist variances in viewing angles and anatomical structures across different retinal images, keypoint-based approaches become the mainstream methods for retinal image registration thanks to their robustness and low latency. These methods typically assume the retinal surfaces are planar, and adopt feature matching to obtain the homography matrix that represents the global transformation between images. Yet, such a planar hypothesis inevitably introduces registration errors since retinal surface is approximately curved. This limitation is more prominent when registering image pairs with significant differences in viewing angles. To address this problem, we propose a hybrid registration framework called HybridRetina, which progressively registers retinal images with global and local deformable transformations. For that, we use a keypoint detector and a deformation network called GAMorph to estimate the global transformation and local deformable transformation, respectively. Specifically, we integrate multi-level pixel relation knowledge to guide the training of GAMorph. Additionally, we utilize an edge attention module that includes the geometric priors of the images, ensuring the deformation field focuses more on the vascular regions of clinical interest. Experiments on two widely-used datasets, FIRE and FLoRI21, show that our proposed HybridRetina significantly outperforms some state-of-the-art methods. The code is available at https://github.com/lyp-deeplearning/awesome-retinal-registration.
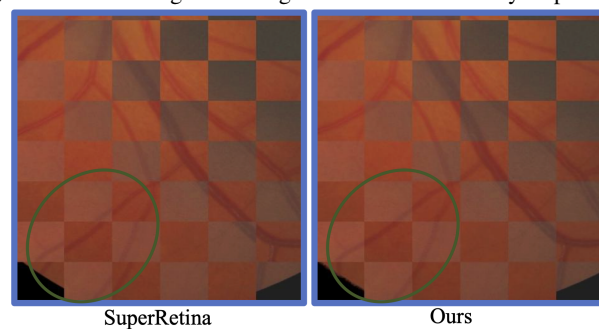
Index Terms—Retinal image registration, retinal image analysis, deformation field, pixel relation guidance

(a) Feature matching result in global transformation by SuperRetina

(b) The registration results of SuperRetina and our proposed method

Fig. 1: An example demonstrates the registration results of the global transformation and our progressive transformation. We use mosaic images to compare the registration performance, and the continuity of blood vessels across tiles reflects the registration quality. SuperRetina [1] exhibits excellent feature matching performance in global transformation, but the registration results still contain obvious errors.

I. INTRODUCTION

According to the World Health Organization, approximately 220 million people worldwide suffer from various degrees of visual impairments, with around 110 million individuals afflicted by preventable eye diseases that have gone untreated [2]. Retinal image registration aims to align multiple images of the same retina obtained from different perspectives and periods. This technique has been substantiated as crucial in medical diagnostics as it enables clinicians to track changes in the retina over time and facilitates precise laser treatment for conditions such as diabetic retinopathy and age-related macular degeneration [1], [3].

Retinal image registration methods can be roughly grouped

* Corresponding Author

into intensity-based and keypoint-based. Intensity-based registration algorithms rely on optimization algorithms to find appropriate matching relationships based on pixel intensities, and are often time-consuming at high resolutions [4]–[7]. With advancements in deep learning, keypoint-based methods have rapidly progressed by learning effective feature representations [1], [8]–[10], as early hand-crafted features struggle to address variations in lighting and anatomy within retinal images [11]–[13].

The keypoint-based methods typically employ keypoint detection and description to find homography transformations between different images. SuperRetina [1] achieves impressive registration performance in retinal image registration by using a semi-supervised training scheme to simultaneously predict keypoints and descriptors. However, keypoint-based methods inherently introduce registration errors due to approximating the retinal surface as planar to calculate the homography transformation. As depicted in Fig. 1, SuperRetina [1] achieves very good feature matching results, but its warped moving image still exhibit many mismatches with the fixed image. Some recent works [14], [15] attempt to obtain vessel masks through additional vessel segmentation and then use nonlinear optimization algorithms to align local regions. However, these approaches introduce additional mask annotation costs and inference time. Directly performing nonlinear alignment on original color fundus images is challenging due to the presence of various background elements outside the blood vessels.

To address this problem, we propose a novel progressive retinal image registration framework called HybridRetina. In the global registration stage, we use a keypoint detector to extract keypoints and calculate the homography matrix, obtaining the coarsely matched image pair. Subsequently, we employ a geometry-aware deformation network, GAMorph, to perform nonlinear alignment for the coarsely matched image pair in the local deformable registration stage. Moreover, we use the **multi-level pixel relation** priors obtained from the global matching stage to guide the movement of pixels in the deformation field. Additionally, we propose an **edge attention module** to ensure that the deformation field focuses more on the alignment of vascular regions. Notably, our deformation field is trained on four open-source color fundus image datasets and tested on both color fundus images and fluorescein angiography images. The results demonstrate the generalization and effectiveness of HybridRetina, outperforming some state-of-the-art performance in retinal image registration.

II. RELATED WORK

A. Global Image Registration

Keypoint-based global registration algorithms typically involve four steps: detection of interest points, computing feature descriptors, feature matching, and estimation of homographic transformation between the images. Many research focus on how to extract more replicable and reliable keypoints [8], [9], [12], [16]. SIFT [11] computes corners and blobs on different scales to achieve scale invariance and extracts descriptors using the local gradients. SuperPoint [8] provides a self-supervised approach to simultaneously train keypoint detection and description. R2D2 [9] learns keypoint detection and description jointly with prediction of the local descriptor discriminativeness to find reliable keypoints.

B. Deformable Image Registration

In the past, there have been numerous non-deep learning nonrigid registration algorithms. Several studies optimize within the space of displacement vector fields. Daniel *et al.* [17] use affine transformations for global motion matching and use free-form deformation based by B-splines to describe local variations. Tom *et al.* [18] adapt the optimization procedure underlying the Demons algorithm to a space of diffeomorphic transformations. With the rise of deep learning techniques, there has been an emergence of registration algorithms based on deep learning [19]–[24]. The initial algorithms were trained based on supervised labels [25], [26]. However, these supervised algorithms typically require deformation fields as ground truth. Subsequently, unsupervised deformation fields gained prominence. Voxelmorph [19] rapidly computes a deformation field by unsupervised training from coarsely aligned data. TransMorph [20] uses a hybrid Transformer-ConvNet model and achieves better registration results on image pairs with substantial deformations. Although these unsupervised methods such as VoxelMorph and TransMorph have shown to be promising for image registration, it is challenging to apply them to retinal images, as retinal image registration requires precise alignment in many regions such as the vessel area.

C. Retina Image Registration

Most of existing retinal image registration methods are based on rigid transformation [3], [27], [28]. LoSPA [29] and DeepSPA [30] focus on describing image patches by step pattern analysis for homography estimation. REMPE [31] first finds many candidate points by vessel bifurcation detection and the SIFT detector [11], and then performs point pattern matching based on eye modelling and camera pose estimation to identify geometrically valid matches. SuperRetina [1] proposes progressive keypoint expansion to enrich the keypoint labels at each training epoch. By utilizing a keypoint-based improved triplet loss as its description loss, SuperRetina produces highly discriminative descriptors. GeoFormer [32] is trained in a fully self-supervised manner by minimizing a multi-scale cross entropy based matching loss on auto-generated training data.

In this paper, we propose to integrate rigid registration with deformable models for retinal image registration.

III. METHOD

The keypoint-based algorithms are unable to handle the geometric distortions that occur when mapping the nearly spherical retinal surface onto the image plane. To address this issue, we propose a progressive retinal image registration framework. In this section, we first introduce the progressive
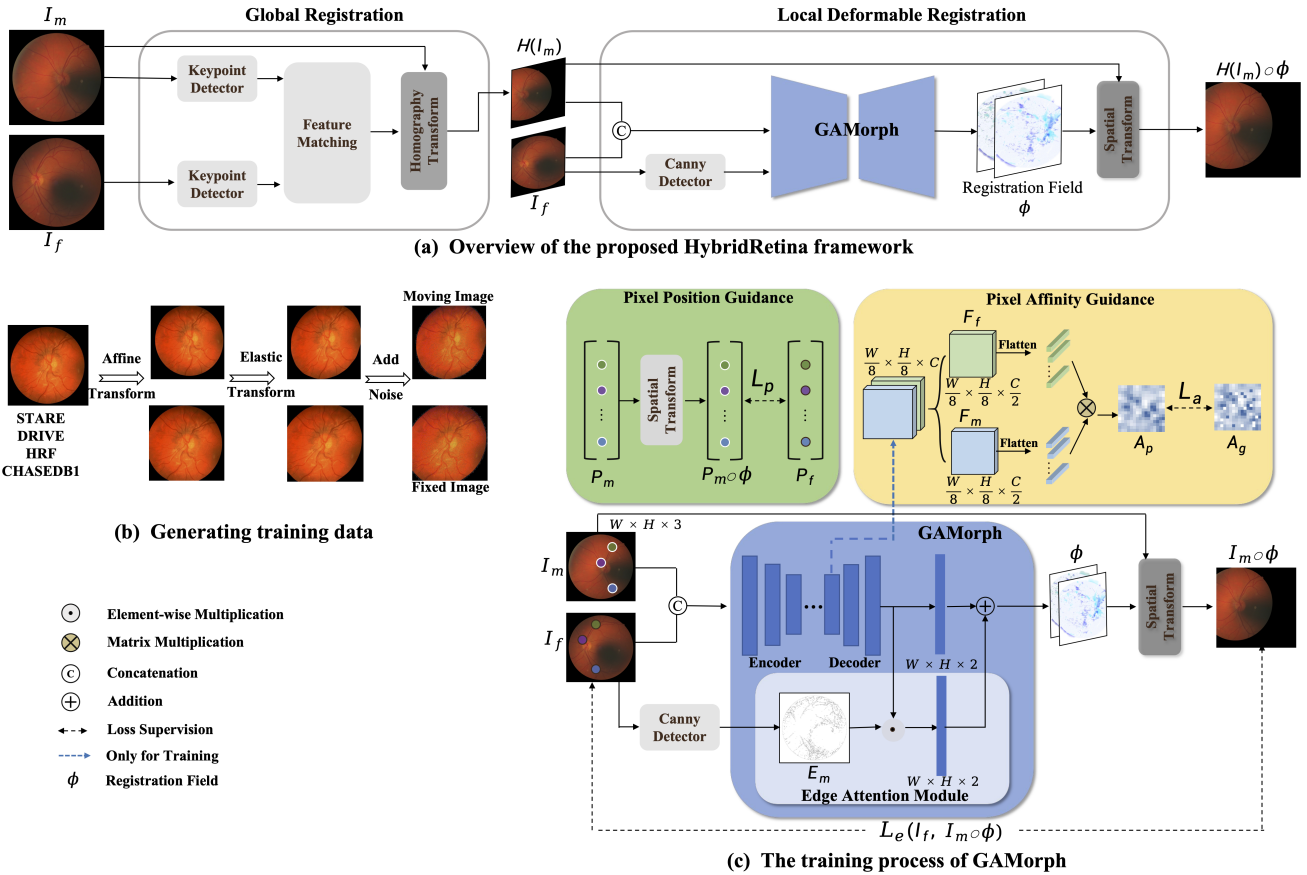
Fig. 2: Illustration of Our HybridRetina Framework. (a) The steps of global registration and local deformable registration. (b) The process of generating paired data for our proposed GAMorph. (c) The training process of GAMorph.

registration process (Sec. III-A). Next, we introduce our proposed multi-level pixel relation guidance (Sec. III-B) and edge attention module (Sec. III-C), which assist in the training of our deformation field prediction network, GAMorph. Finally, we introduce the loss function of GAMorph (Sec. III-D).

A. Progressive Registration

Fig. 2.a illustrates the process of our progressive registration framework. Given the source moving image $I_m \in \mathbb{R}^{W \times H \times 3}$ and the fixed target image $I_f \in \mathbb{R}^{W \times H \times 3}$, we first use a keypoint detector to extract keypoints and corresponding descriptors. Descriptors are matched using the nearest neighbor algorithm in feature matching stage. Subsequently, the RANSAC algorithm is utilized to obtain the global homography transformation matrix between the image pair, transforming the moving image I_m into $H(I_m)$. The output of the global registration is fed into the network GAMorph to predict the registration field $\phi \in \mathbb{R}^{W \times H \times 2}$. Finally, we utilize the spatial transform operation [33] to get the warped moving image $I_m \circ \phi$.

We use the pre-trained SuperRetina [1] network as the keypoint detector to provide the keypoints and descriptors needed for global feature matching in the training stage. It is noteworthy that during the inference phase, we can

use any keypoint detector to replace SuperRetina [1]. The deformation field network GAMorph is based on the UNet architecture, which includes a four-layer encoder and a four-layer decoder to extract features. Then, a prediction head composed of a 3x3 convolutional layer is used to predict the deformation field ϕ. Another branch utilizes the edge attention module, incorporating the geometric priors of the image edges and combining with the deformation field output from the prediction head through an add operation.

B. Multi-level Pixel Relation Guidance

The vanilla deformable registration networks [19], [20] typically assume an equal relationship between pixels. Consequently, they yield suboptimal deformation fields that tend to overfit specific local regions, particularly complex backgrounds. Fortunately, the feature matching results in the global registration stage provides some valuable gifts. In this subsection, we utilize these gifts to establish pixel relationship priors, thereby better supervising the learning of the deformation field.

1) Pixel Affinity Guidance (PAG): The registration field aims to align all pixels of the moving image to the fixed image. We use affinity to describe the degree of association between pixels in the image pair. We observe that matched keypoints information provided by the global registration stage
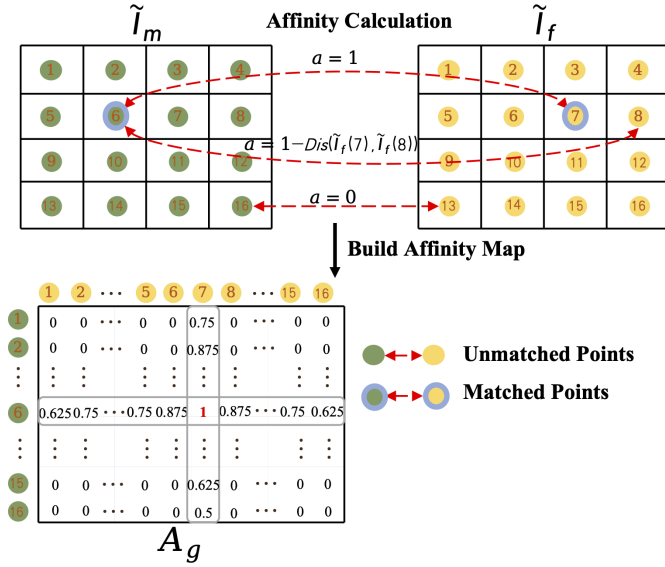
Fig. 3: A toy illustration of computing affinity map A_g. We use matching prior and Manhattan distance to calculate the affinity value a between all pixels.

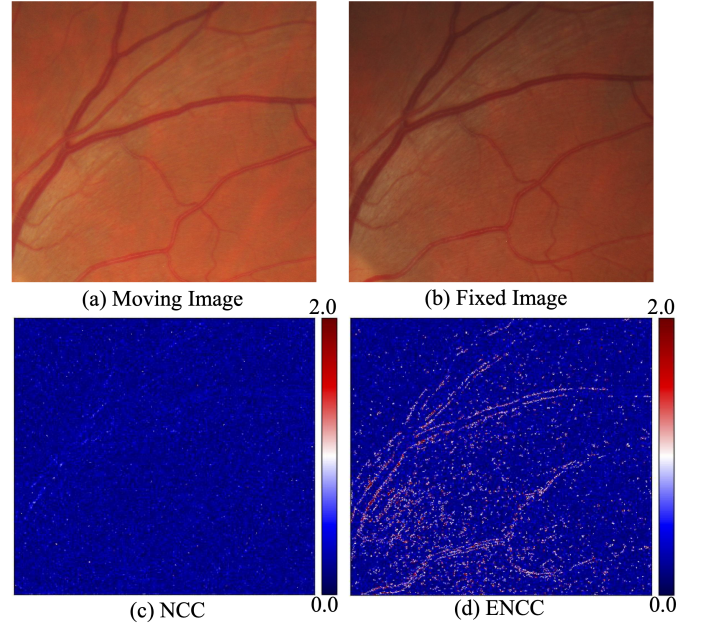(a) Moving Image   (b) Fixed Image

(c) NCC   (d) ENCC

Fig. 4: Comparison of pixel-wise differences between the moving image and the fixed image using different similarity measurement methods. Results of normalized cross-correlation (NCC) and our proposed edge-guided normalized cross-correlation (ENCC) are shown.

offers a pixel relationship prior for the deformation field. These discrete matched keypoints should have a strong affinity value. Additionally, due to the properties of diffeomorphic [19], pixels in the neighborhood of the matched keypoints are also likely to move to the vicinity of the corresponding matched points. Based on these priors, we leverage both the matching information and the Manhattan distance to construct an affinity map A_g between all pixels of the moving image and the fixed image.

As shown in Fig. 3, let $\tilde{I}_m \in \mathbb{R}^{W' \times H' \times 3}$ and $\tilde{I}_f \in \mathbb{R}^{W' \times H' \times 3}$ denote the downsampled moving and fixed images, respectively. In our experiments, we use the downsampling stride of 8, *i.e.*. The ground-truth affinity map $A_g \in \mathbb{R}^{H'W' \times H'W'}$ is then constructed to compute the relationships among all pixels. Let the pixel points in $\tilde{I}_m$ and $\tilde{I}_f$ be represented by (x_i, y_i) and (x_j, y_j), respectively. The elements $A_g(i, j)$ of the affinity relationship matrix A_g are computed as follows:

$$A_g(i,j) = \begin{cases} 1, & \text{if } (x_i, y_i) \text{ matches } (x_j, y_j) \\ 1 - \|(x_j, y_j) - (x_m, y_m)\|_1, & \text{if } (x_i, y_i) \text{ matches } (x_m, y_m) \text{ in } \tilde{I}_f \\ 1 - \|(x_n, y_n) - (x_i, y_i)\|_1, & \text{if } (x_n, y_n) \text{ in } \tilde{I}_m \text{ matches } (x_j, y_j) \\ 0, & \text{otherwise} \end{cases} \tag{1}$$

where $\| \cdot \|_1$ indicates the normalized Manhattan distance.

To obtain the predicted affinity map, we employ an affinity prediction branch that exists only during the training phase as depicted in Fig. 2.c. Specifically, we directly split the feature map obtained from the decoder into F_m and F_f, representing the pixels of moving image and fixed image, respectively. Then, we flatten the feature maps F_m and F_f and conduct matrix multiplication, *i.e.*, the predicted affinity map is computed as $A_p = F_m F_f^\top \in \mathbb{R}^{H'W' \times H'W'}$. Lastly, we

evaluate the loss between the predicted and the ground-truth affinity maps as follows:

$$L_a = \mathcal{L}_{mse}(A_p, A_g). \tag{2}$$

2) Pixel Position Guidance (PPG): The position information of the matched keypoint pairs can explicitly supervise the local predictions of the deformation field. However, it should be noted that the keypoint positions from the keypoint detector may not be entirely accurate, as the detector uses Non-Maximum Suppression (NMS) to identify local maximum response points. We observe that keypoints with prominent geometric features in an image are often more reliable, such as points on blood vessels. Therefore, we calculate the sum of horizontal and vertical gradients for keypoints on the reference image and select the top 120 keypoints as the supervisory signal. Let $P_m \in \mathbb{R}^{N \times 2}$ and $P_f \in \mathbb{R}^{N \times 2}$ denote the selected keypoints from the moving image and the fixed image, respectively. The loss for local pixel position guidance can be defined as:

$$L_p = \mathcal{L}(P_m \circ \phi, P_f), \tag{3}$$

where $\mathcal{L}$ represents the smooth-ℓ_1 loss function defined in [34], and $P_m \circ \phi$ represents the corresponding keypoints in warped moving image obtained by the registration field ϕ.

C. Edge Attention Module

Learning deformation fields involves minimizing pixel-wise differences while preserving diffeomorphic properties. However, commonly used similarity loss functions such as

normalized cross-correlation (NCC) [19] tend to prioritize global similarity at the expense of local fine-grained alignment. As shown in Fig. 2.c, we propose an edge attention module to emphasize the importance of edge priors for improved local fine-grained alignment. Specifically, we first employ the Canny detector [35] with adaptive thresholds to extract edges from the fixed image. Then, we derive a binary edge mask E_m and add it to the output of the decoder to obtain the final deformation field that includes edge priors. In addition, we propose a new edge-guided NCC (ENCC) loss L_e by integrating edge mask with the original NCC loss [19].

As shown in Fig. 4, our proposed ENCC loss focuses more on changes in blood vessels and assigns greater weight to the edge response regions, making it more similar to clinical diagnosis. For training, we need to minimize the error between the fixed image I_f and the warped moving image $I_t = (I_m \circ \phi)$. The loss function L_e is calculated as follows:

$$L_e = \sum_p \frac{(1 + E_m(p)) \left(\sum_{p_i \in \Omega_p} \left(I_f(p_i) - \bar{I}_f(p) \right) \left(I_t(p_i) - \bar{I}_t(p) \right) \right)^2}{\left(\sum_{p_i \in \Omega_p} \left(I_f(p_i) - \bar{I}_f(p) \right)^2 \right) \left(\sum_{p_i \in \Omega_p} \left(I_t(p_i) - \bar{I}_t(p) \right)^2 \right)},$$

(4)

where Ω_p denotes the set of neighboring points near point p, and $\bar{I}_f$ and $\bar{I}_t$ denotes mean values within local $w \times w$ ($w = 15$) window centered at p.

D. Overall Loss

As shown in Fig. 2.b, we use the open-source color fundus retinal images to construct the training image pairs. The multi-level pixel relation guidance module generates the losses L_a and L_p. Meanwhile, the similarity loss L_e is obtained by applying the ENCC loss function to the warped moving image and the fixed image. Finally, we also incorporate regularization terms L_{smooth} inspired by VoxelMorph [19], which enforces a spatially smooth deformation as a function of the spatial gradients of registration field. The overall loss function is as follows:

$$L_{all} = L_a + \lambda_1 L_p + \lambda_2 L_e + \lambda_3 L_{smooth},$$

(5)

where λ_1, λ_2, and λ_3 are employed to balance different loss terms. In our experiments, we empirically set $\lambda_1 = 5.0$, $\lambda_2 = 2.0$, and $\lambda_3 = 1.0$ to ensure that all loss terms exhibit similar gradient norms.

IV. EXPERIMENTS

A. Datasets and Evaluation Metrics

Our model is trained on four public color fundus datasets and tested on two challenging retinal registration datasets.
The Training dataset: We utilize four publicly available retinal color fundus datasets, including STARE [38], DRIVE [39], CHASEDB1 [40], and HRF [41], totaling 768 images without annotated keypoints.
The FIRE dataset:[1] [36] The first public test set we used is the FIRE dataset, which has 134 registered color fundus image pairs of size 2912×2912 acquired by a Nidek AFC210

fundus camera. The images are split into three categories with different characteristics: 1) Category-$\mathcal{S}$ contains 71 pairs with large overlaps and no anatomical changes, making them easy to register; 2) Category-$\mathcal{A}$ contains 14 pairs with large overlaps and significant anatomical changes, making them moderately hard to register; and 3) Category-$\mathcal{P}$ contains 49 pairs with small overlaps, making them hard to register. Each pair of images is manually annotated with 10 pairs of points, primarily located at vessel junctions and intersections.
The FLORI21 dataset:[2] [42] The second public test set we used is the FLORI21 dataset, which provides 15 pairs of ultra-widefield (UWF) fluorescein angiography images. The fluorescein angiography images have a large field of view (FOV) up to $200°$ compared to narrow-field images (between $30°$ and $50°$). Each pair of images is annotated with 15 pairs of points at vessel birucations, ensuring coverage of the entire image area.
Evaluation Metrics. Each image pair is annotated with at least 10 pairs of points distributed globally across the image. Following [1], we measure the registration performance based on the root mean square error (RMSE) , acceptable rate (Accept) and area under curve (AUC) metrics.

Let K_f denote the ground truth points on the fixed image, and K'_m represent the ground truth points on the moving image after being transformed by the registration algorithm. We first calculate the RMSE metric between K_f and K'_m. Next, we calculate the acceptable rate for all images, where a case is considered successful if RMSE < 20. Finally, we calculate the AUC metric [36], which requires computing the expectation of success rate at different threshold values of RMSE.

B. Implementation Details

We implement the proposed GAMorph using PyTorch. The models are trained on a single NVIDIA GeForce RTX 2080 Ti GPU, and all input images are resized to 768×768 pixels. We employ the extensively utilized Adam optimizer, setting a learning rate of 0.001 and a batch size of 8. To generate paired training images, we apply random affine transformations, including rotation, translation, and scaling. Additionally, we utilize elastic transformations [43] to introduce deformations in the images, specifically using an intensity value of 50 and a standard deviation of 6 for the Gaussian filter kernel to ensure appropriate elastic deformation. Finally, we add Gaussian noise to increase the differences between pixels.

C. Performance Results on FIRE

We mainly compare with two types of state-of-the-art methods on the FIRE dataset:

- Traditional algorithms: SIFT [11], PBO [7] and REMPE [31].
- Deep learning-based methods: GLAMPoints [3], Super-Glue [37], R2D2 [9], NCNet [44], SuperRetina [1], and GeoFormer [32] .

---

[1]https://projects.ics.forth.gr/cvrl/fire/

[2]https://ieee-dataport.org/open-access/

TABLE I: Quantitative comparison with state-of-the-art methods for color fundus image registration on the FIRE dataset [36]. We present the results of GAMorph with different keypoint detectors. The performance improvements of our method over the baseline are marked in blue.

Method	RMSE↓	Accept [%]↑	AUC-$\mathcal{S}$ [%]↑	AUC-$\mathcal{A}$ [%]↑	AUC-$\mathcal{P}$ [%]↑	mAUC [%]↑
PBO, ICIP2010 [7]	18.6	70.9	84.4	69.1	12.2	55.2
REMPE, JBHI2020 [31]	6.3	97.0	95.8	66.0	54.2	72.0
GLAMpoints, ICCV2019 [3]	13.6	92.5	85.0	54.3	47.4	62.2
SuperGlue, CVPR2020 [37]	9.4	95.5	88.5	68.9	48.8	68.7
R2D2, NIPS2019 [9]	6.4	95.5	92.8	66.6	54.0	71.1
NCNet, TPAMI2022 [1]	14.1	85.8	81.7	60.9	41.0	61.2
SIFT, IJCV04 [11]	17.2	79.9	90.3	47.4	34.1	57.3
SIFT [11] + GAMorph	12.5 (-4.7)	89.5 (+9.6)	91.0 (+0.7)	56.8 (+9.4)	42.1 (+8.0)	63.3 (+6.0)
SuperPoint, CVPRW2018 [8]	11.8	94.8	89.3	68.0	43.4	66.9
SuperPoint [8] + GAMorph	6.2 (-5.6)	97.0 (+2.2)	89.7 (+0.4)	71.7 (+3.7)	55.0 (+11.6)	72.2 (+5.3)
SuperRetina, ECCV2022 [1]	5.2	98.5	94.0	78.3	54.2	75.5
SuperRetina [1] + GAMorph	4.5 (-0.7)	99.2 (+0.7)	94.4 (+0.4)	80.6 (+2.3)	65.9 (+11.7)	80.3 (+4.8)
GeoFormer, ICCV2023 [32]	5.2	98.5	94.4	76.6	55.9	75.6
GeoFormer [32] + GAMorph	**4.5** (-0.7)	**99.2** (+0.7)	**95.8** (+1.4)	**80.6** (+4.0)	**66.3** (+10.4)	**80.9** (+5.3)

TABLE II: Quantitative comparison of the proposed HybridRetina with state-of-the-art methods on the FLoRI21 dataset [42]. We present the results of GAMorph with different keypoint detectors. The performance improvements of our method over the baseline are marked in blue.

Methods	RMSE ↓	Accept [%] ↑	AUC [%] ↑
REMPE [31]	35.9	46.7	56.8
SIFT [11]	44.8	33.3	48.2
SIFT [39] + GAMorph	38.7 (-6.1)	40.0 (+6.7)	54.1 (+5.9)
SuperPoint [8]	23.7	73.3	68.3
SuperPoint [39] + GAMorph	19.2 (-4.5)	73.3 (+0.0)	74.8 (+6.5)
SuperRetina [1]	18.0	80.0	77.1
SuperRetina [39] + GAMorph	13.1 (-4.9)	86.7 (+6.7)	84.3 (+7.2)
GeoFormer [32]	17.2	80.0	78.2
GeoFormer [32] + GAMorph	**12.5** (-4.7)	**86.7** (+6.7)	**84.8** (+6.6)

TABLE III: Ablation study on key components of GAMorph. These experiments use SuperRetina as the keypoint detector and adopt the AUC [%] for FIRE and FLORI21 datasets.

Baseline	PAG	PPG	EAM	FIRE	FLORI21
✓				75.9	77.9
✓	✓			77.1	79.6
✓	✓	✓		78.7	82.1
✓	✓	✓	✓	80.3	84.3

In Tab. I, we demonstrate the results of our HybridRetina framework using four different keypoint detectors. It can be observed that our proposed GAMorph improves these baselines on mAUC metric by 6.0%, 5.3%, 4.8% and 5.3%, respectively. It is noteworthy that GAMorph only uses Super-Retina as the keypoint detector during training, and does not require fine-tuning when paired with other keypoint detectors.

Our HybridRetina achieves the highest mAUC of 80.9% when using GeoFormer [1] as the keypoint detector. Compared with the best traditional method REMPE [31], we achieve the same AUC in the easy subset $\mathcal{S}$. However, REMPE struggles with the $\mathcal{A}$ subset, which has significant anatomical changes, and the $\mathcal{P}$ subset, which has small overlap. Moreover, REMPE requires three minutes to register each image pair, whereas our GAMorph only requires 32 milliseconds. It is noteworthy that our algorithm achieves the best overall performance in both challenging subsets, $\mathcal{A}$ and $\mathcal{P}$. Visualized checkerboard images in Fig. 5 highlight our method's superior alignment compared to GeoFormer [32].

D. Performance Results on FLORI21

The FLORI21 dataset presents challenges due to significant scale differences and small overlaps between images. Addi-

tionally, our deformation network GAMorph is trained using only color fundus images, and it has not seen fluorescein angiography images. As shown in Tab.II, our method improves the AUC by 5.9%, 6.5%, 7.2%, and 6.6% for the four global registration detectors, respectively.

E. Ablation Studies

To justify the effectiveness and robustness of our proposed geometry guidance, we conduct a set of ablation studies on the FIRE dataset and FLoRI21 dataset. In these experiments, we utilize SuperRetina as the keypoint detector.

Ablation study on key components of GAMorph. We perform ablation study to evaluate each individual module's influence. Our baseline includes only the NCC loss function and the regularization term L_{smooth}. As dedicated in Tab. III, all the three components significantly contribute to the Hy-bridRetina. Pixel affinity guidance (PAG) improves the AUC by 1.2% and 1.7%, respectively. Pixel position guidance (PPG) improves the AUC by 1.6% and 2.5%, respectively. Edge attention module (EAM) and the ENCC loss function together improve the AUC by 1.6% and 2.2%, respectively.

Ablation study on using different deformable methods. We compare our GAMorph with other traditional and deep learning-based deformable methods. To ensure a fair comparison, we retrained deep learning networks VoxelMorph [19], AC-RegNet [45], and TransMorph [20] on our training dataset. As shown in Tab. IV, our proposed GAMorph achieves the best performance, outperforming TransMorph by 2.9% on the FIRE dataset and by 3.1% on the FLORI21 dataset.
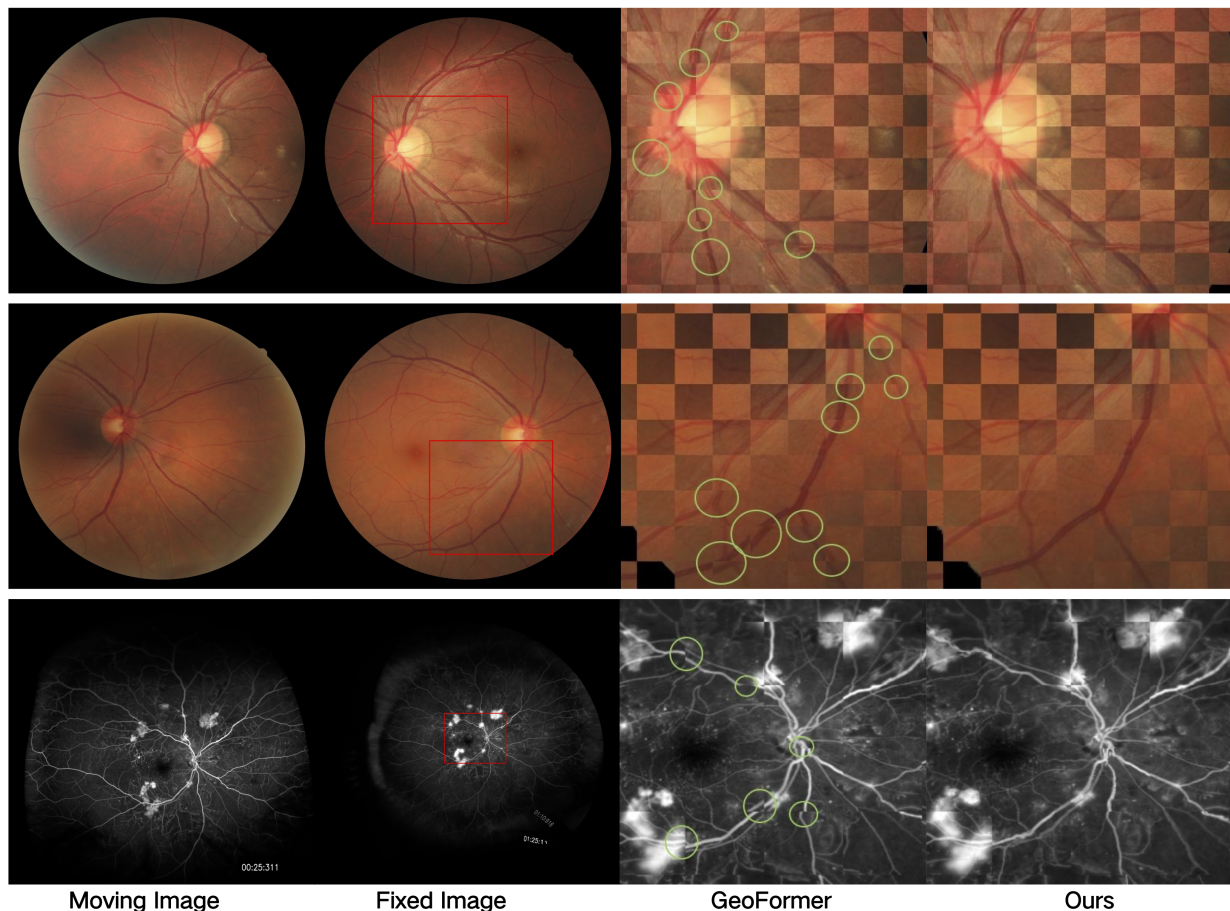
Fig. 5: Mosaic visualization of registration results. We show the alignment in the region enclosed by the red box. We observe misalignment in the results by GeoFormer [32], highlighted by green circles. Best viewed electronically.

TABLE IV: Ablation study on using different deformable methods. The baseline directly uses the global matching results obtained from SuperRetina, while the other deformable methods are applied to the images after global registration.

Methods	FIRE	FLORI21
SuperRetina, ECCV2022 [1]	75.5	77.1
SuperRetina + Diff Demons, NeuroImage2009 [18]	76.1	79.0
SuperRetina + VoxelMorph, TMI2019 [19]	76.4	79.8
SuperRetina + AC-RegNet, Neural Netw2020 [45]	75.8	78.6
SuperRetina + Transmorph [20], MIA2022	77.4	81.2
SuperRetina + GAMorph (proposed)	**80.3**	**84.3**

F. Runtime Analysis

The run time of network is computed over 134 pairs of images with a resolution of 768×768 pixels. We validate the efficiency of our algorithm on an NVIDIA GeForce RTX 3090 GPU. Our HybridRetina framework, combining SuperRetina and GAMorph, achieves an average processing time of 85ms per image, with GAMorph only requiring 32ms.

V. CONCLUSION

Retinal image registration typically relies on a global homography transformation using keypoints and their descrip-

tions. To further improve the accuracy of global transformation methods, we propose a progressive registration framework that includes both global registration and local deformable registration. Our method significantly improves the performance of state-of-the-art algorithms on two widely used datasets. In the future, we would like to explore the potential of our method in multimodal medical image registration.

REFERENCES

[1] J. Liu, X. Li, Q. Wei, J. Xu, and D. Ding, "Semi-supervised keypoint detector and descriptor for retinal image matching," in *ECCV*, 2022, pp. 593–609.

[2] D. Motta, W. Casaca, and A. Paiva, "Vessel optimal transport for automated alignment of retinal fundus images," *IEEE Trans. on Image Processing*, vol. 28, no. 12, pp. 6154–6168, 2019.

[3] P. Truong, S. Apostolopoulos, A. Mosinska, S. Stucky *et al.*, "Glampoints: Greedily learned accurate match points," in *CVPR*, 2019, pp. 10 732–10 741.

[4] J. Chen, J. Tian, N. Lee, J. Zheng, R. T. Smith, and A. F. Laine, "A partial intensity invariant feature descriptor for multimodal retinal image registration," *IEEE Trans. on Biomedical Engineering*, vol. 57, no. 7, pp. 1707–1718, 2010.

[5] M. Zaslavskiy, F. Bach, and J.-P. Vert, "A path following algorithm for the graph matching problem," *IEEE Trans. on Pattern Anal. and Mach. Intell.*, vol. 31, no. 12, pp. 2227–2242, 2008.

[6] N. Ritter, R. Owens, J. Cooper, R. H. Eikelboom, and P. P. Van Saarloos, "Registration of stereo and temporal images of the retina," *IEEE Trans. on Medical Imaging*, vol. 18, no. 5, pp. 404–418, 1999.

[7] H. Oinonen, H. Forsvik, P. Ruusuvuori, O. Yli-Harja, V. Voipio, and H. Huttunen, "Identity verification based on vessel matching from fundus images," in *Proc. of IEEE Intl. Conf. on Image Processing*, 2010, pp. 4089–4092.

[8] D. DeTone, T. Malisiewicz, and A. Rabinovich, "Superpoint: Self-supervised interest point detection and description," in *Proc. of IEEE Conf. on Computer Vision and Pattern Recognition Workshops*, 2018, pp. 224–236.

[9] J. Revaud, C. De Souza, M. Humenberger, and P. Weinzaepfel, "R2d2: Reliable and repeatable detector and descriptor," *Proc. of Advances in Neural Information Processing Systems*, vol. 32, 2019.

[10] Y. Liu, Z. Gu, S. Gao, D. Wang, Y. Zeng, and J. Cheng, "Mos: A low latency and lightweight framework for face detection, landmark localization, and head pose estimation," in *Proc. of British Machine Vision Conference*, 2021, p. 266.

[11] L. David, "Distinctive image features from scale-invariant keypoints," *Intl. Journal of Computer Vision*, vol. 60, pp. 91–110, 2004.

[12] H. Bay, T. Tuytelaars, and L. Van Gool, "Surf: Speeded up robust features," in *ECCV*, 2006, pp. 404–417.

[13] P. C. Cattin, H. Bay, L. Van Gool, and G. Székely, "Retina mosaicing using local features," in *Proc. of Intl. Conf. on Medical Image Computing and Computer Assisted Intervention*, 2006, pp. 185–192.

[14] L. Ding, T. D. Kang, A. E. Kuriyan, R. S. Ramchandran, C. C. Wykoff, and G. Sharma, "Combining feature correspondence with parametric chamfer alignment: Hybrid two-stage registration for ultra-widefield retinal images," *IEEE Trans. on Biomedical Engineering*, vol. 70, no. 2, pp. 523–532, 2022.

[15] J. Zhang, Y. Wang, J. Dai, M. Cavichini, D.-U. G. Bartsch, W. R. Freeman, T. Q. Nguyen, and C. An, "Two-step registration on multi-modal retinal images via deep neural networks," *IEEE Transactions on Image Processing*, vol. 31, pp. 823–838, 2021.

[16] G. Potje, F. Cadar, A. Araujo, R. Martins, and E. R. Nascimento, "Enhancing deformable local features by jointly learning to detect and describe keypoints," in *CVPR*, 2023, pp. 1306–1315.

[17] D. Rueckert, L. I. Sonoda, C. Hayes, D. L. Hill, M. O. Leach, and D. J. Hawkes, "Nonrigid registration using free-form deformations: application to breast mr images," *IEEE Trans. on Medical Imaging*, vol. 18, no. 8, pp. 712–721, 1999.

[18] T. Vercauteren, X. Pennec, A. Perchant, and N. Ayache, "Diffeomorphic demons: Efficient non-parametric image registration," *NeuroImage*, vol. 45, no. 1, pp. S61–S72, 2009.

[19] G. Balakrishnan, A. Zhao, M. R. Sabuncu, J. Guttag, and A. V. Dalca, "Voxelmorph: a learning framework for deformable medical image registration," *IEEE Trans. on Medical Imaging*, vol. 38, no. 8, pp. 1788–1800, 2019.

[20] J. Chen, E. C. Frey, Y. He, W. P. Segars, Y. Li, and Y. Du, "Transmorph: Transformer for unsupervised medical image registration," *Medical image analysis*, vol. 82, p. 102615, 2022.

[21] J. Shi, Y. He, Y. Kong *et al.*, "Xmorpher: Full transformer for deformable medical image registration via cross attention," in *Proc. of Intl. Conf. on Medical Image Computing and Computer Assisted Intervention*, 2022, pp. 217–226.

[22] X. Fan, Z. Li, Z. Li, X. Wang, R. Liu, Z. Luo, and H. Huang, "Automated learning for deformable medical image registration by jointly optimizing network architectures and objective functions," *IEEE Transactions on Image Processing*, 2023.

[23] H. Wang, D. Ni, and Y. Wang, "Recursive deformable pyramid network for unsupervised medical image registration," *IEEE Transactions on Medical Imaging*, 2024.

[24] Z. Chen, Y. Zheng, and J. C. Gee, "Transmatch: a transformer-based multilevel dual-stream feature matching network for unsupervised deformable image registration," *IEEE Transactions on Medical Imaging*, 2023.

[25] H. Sokooti, B. De Vos, F. Berendsen, B. P. Lelieveldt, I. Išgum, and M. Staring, "Nonrigid image registration using multi-scale 3d convolutional neural networks," in *Proc. of Intl. Conf. on Medical Image Computing and Computer Assisted Intervention*, 2017, pp. 232–239.

[26] X. Yang, R. Kwitt, M. Styner, and M. Niethammer, "Quicksilver: Fast predictive image registration–a deep learning approach," *NeuroImage*, vol. 158, pp. 378–396, 2017.

[27] K. Deng, J. Tian, J. Zheng, X. Zhang, X. Dai, and M. Xu, "Retinal fundus image registration via vascular structure graph matching," *Journal of Biomedical Imaging*, vol. 2010, pp. 1–13, 2010.

[28] D. Braun, S. Yang, J. N. Martel, C. N. Riviere, and B. C. Becker, "Eyeslam: Real-time simultaneous localization and mapping of retinal vessels during intraocular microsurgery," *The International Journal of Medical Robotics and Computer Assisted Surgery*, vol. 14, no. 1, p. e1848, 2018.

[29] J. Addison Lee, J. Cheng, B. Hai Lee, E. Ping Ong, G. Xu, D. Wing Kee Wong, J. Liu, A. Laude, and T. Han Lim, "A low-dimensional step pattern analysis algorithm with application to multimodal retinal image registration," in *CVPR*, 2015, pp. 1046–1053.

[30] J. A. Lee, P. Liu, J. Cheng, and H. Fu, "A deep step pattern representation for multimodal retinal image registration," in *CVPR*, 2019, pp. 5077–5086.

[31] C. Hernandez-Matas, X. Zabulis, and A. A. Argyros, "Rempe: Registration of retinal images through eye modelling and pose estimation," *IEEE Journal of Biomedical and Health Informatics*, vol. 24, no. 12, pp. 3362–3373, 2020.

[32] J. Liu and X. Li, "Geometrized transformer for self-supervised homography estimation," in *CVPR*, 2023, pp. 9556–9565.

[33] M. Jaderberg, K. Simonyan, A. Zisserman *et al.*, "Spatial transformer networks," *Proc. of Advances in Neural Information Processing Systems*, vol. 28, 2015.

[34] S. Ren, K. He, R. Girshick, and J. Sun, "Faster r-cnn: Towards real-time object detection with region proposal networks," *Proc. of Advances in Neural Information Processing Systems*, vol. 28, 2015.

[35] J. Canny, "A computational approach to edge detection," *IEEE Trans. on Pattern Anal. and Mach. Intell.*, pp. 679–698, 1986.

[36] C. Hernandez-Matas, X. Zabulis, A. Triantafyllou, P. Anyfanti, S. Douma, and A. A. Argyros, "Fire: fundus image registration dataset," *Journal for Modeling in Ophthalmology*, vol. 1, no. 4, pp. 16–28, 2017.

[37] P.-E. Sarlin, D. DeTone, T. Malisiewicz, and A. Rabinovich, "Superglue: Learning feature matching with graph neural networks," in *CVPR*, 2020, pp. 4938–4947.

[38] A. Hoover and M. Goldbaum, "Locating the optic nerve in a retinal image using the fuzzy convergence of the blood vessels," *IEEE Trans. on Medical Imaging*, vol. 22, no. 8, pp. 951–958, 2003.

[39] J. Staal, M. D. Abràmoff, M. Niemeijer, M. A. Viergever, and B. Van Ginneken, "Ridge-based vessel segmentation in color images of the retina," *IEEE Trans. on Medical Imaging*, vol. 23, no. 4, pp. 501–509, 2004.

[40] M. M. Fraz, P. Remagnino, A. Hoppe, B. Uyyanonvara *et al.*, "An ensemble classification-based approach applied to retinal blood vessel segmentation," *IEEE Trans. on Biomedical Engineering*, vol. 59, no. 9, pp. 2538–2548, 2012.

[41] J. Odstrčilík, J. Jan, J. Gazárek, and R. Kolář, "Improvement of vessel segmentation by matched filtering in colour retinal images," in *World Congress on Medical Physics and Biomedical Engineering*, 2009, pp. 327–330.

[42] L. Ding *et al.*, "Flori21: Fluorescein angiography longitudinal retinal image registration dataset," *IEEE Dataport*, 2021.

[43] P. Y. Simard, D. Steinkraus, J. C. Platt *et al.*, "Best practices for convolutional neural networks applied to visual document analysis." in *Proc. of International Conference on Document Analysis and Recognition*, vol. 3, 2003.

[44] I. Rocco, M. Cimpoi, R. Arandjelović, A. Torii, T. Pajdla, and J. Sivic, "Ncnet: Neighbourhood consensus networks for estimating image correspondences," *IEEE Transactions on Pattern Analysis and Machine Intelligence*, vol. 44, no. 2, pp. 1020–1034, 2020.

[45] L. Mansilla, D. H. Milone, and E. Ferrante, "Learning deformable registration of medical images with anatomical constraints," *Neural Networks*, vol. 124, pp. 269–279, 2020.